Title

Exploring the Pullback Attractors of a Low-Order Quasigeostrophic Ocean Model: The Deterministic Case

Journal

Journal of Climate, 29(11)

ISSN

0894-8755

Authors

Pierini, Stefano
Ghil, Michael
Chekroun, Mickael D

Publication Date

2016-06-01

DOI

10.1175/jcli-d-15-0848.1

Peer reviewed

Pierini al'16

Data · August 2016

CITATIONS
0

READS
30

3 authors:

Stefano Pierini
Parthenope University of Naples
81 PUBLICATIONS **614** CITATIONS
SEE PROFILE

Michael Ghil
Ecole Normale Supérieure, Paris
565 PUBLICATIONS **18,081** CITATIONS
SEE PROFILE

Mickael David Chekroun
University of California, Los Angeles
66 PUBLICATIONS **438** CITATIONS
SEE PROFILE

Exploring the Pullback Attractors of a Low-Order Quasigeostrophic Ocean Model: The Deterministic Case

STEFANO PIERINI

Universitá di Napoli Parthenope, Napoli, Italy

MICHAEL GHIL

Ecole Normale Supérieure, Paris, France, and University of California, Los Angeles, Los Angeles, California

MICKAEL D. CHEKROUN

University of California, Los Angeles, Los Angeles, California

(Manuscript received 30 November 2015, in final form 1 March 2016)

ABSTRACT

A low-order quasigeostrophic double-gyre ocean model is subjected to an aperiodic forcing that mimics time dependence dominated by interdecadal variability. This model is used as a prototype of an unstable and nonlinear dynamical system with time-dependent forcing to explore basic features of climate change in the presence of natural variability. The study relies on the theoretical framework of nonautonomous dynamical systems and of their pullback attractors (PBAs), that is, of the time-dependent invariant sets attracting all trajectories initialized in the remote past. The existence of a global PBA is rigorously demonstrated for this weakly dissipative nonlinear model. Ensemble simulations are carried out and the convergence to PBAs is assessed by computing the probability density function (PDF) of localization of the trajectories. A sensitivity analysis with respect to forcing amplitude shows that the PBAs experience large modifications if the underlying autonomous system is dominated by small-amplitude limit cycles, while less dramatic changes occur in a regime characterized by large-amplitude relaxation oscillations. The dependence of the attracting sets on the choice of the ensemble of initial states is then analyzed. Two types of basins of attraction coexist for certain parameter ranges; they contain chaotic and nonchaotic trajectories, respectively. The statistics of the former does not depend on the initial states whereas the trajectories in the latter converge to small portions of the global PBA. This complex scenario requires separate PDFs for chaotic and nonchaotic trajectories. General implications for climate predictability are finally discussed.

1. Introduction and motivation

Weather and climate predictability have been investigated for several decades, starting from the pioneering work of Lorenz (1963), by relying on the concepts and methods of autonomous dissipative nonlinear dynamical systems (Ghil and Childress 1987, and references therein). For such systems, any initial volume in phase space contracts in time, on the average, thus eventually reducing to a time-invariant set of zero volume called an attractor. In the autonomous case, an attractor can be a fixed point, a limit cycle, an invariant torus, or a strange attractor (Eckmann and Ruelle 1985; Ott 2002; Tél and Gruiz 2006).

Investigating a system's attractors, in particular the strange attractors that describe the statistical properties of deterministic chaos, is fundamental in this context (Eckmann and Ruelle 1985) and has helped considerably in the study of multiple weather regimes and of their predictability on time scales of weeks to months (Ghil and Robertson 2002, and references therein). On the other hand, when studying the longer time scales—interannual, interdecadal, and longer—that are associated with climate change, it becomes necessary to take into consideration the time dependence of both anthropogenic

Corresponding author address: Stefano Pierini, Dipartimento di Scienze e Tecnologie, Universitá di Napoli Parthenope, Centro Direzionale, Isola C4, 80143 Napoli, Italy.
E-mail: stefano.pierini@uniparthenope.it

DOI: 10.1175/JCLI-D-15-0848.1

and natural forcing (Martinson et al. 1995; Mann et al. 1998; Chang et al. 2015). The proper framework for studying changes in the system's internal variability, and not just in its mean properties, when subject to variable forcing is that of nonautonomous and random dynamical systems (Drótos et al. 2015; Ghil 2015, 2016).

In the latter framework, the natural generalization of the attractors is provided by pullback attractors (PBAs). A global PBA is defined in the mathematical literature as a time-dependent set $\mathscr{A}(t)$ in the system's phase space X that is invariant under its governing equations—together with the equally time-dependent, invariant measure $\mu(t)$ supported on this set—and to which all trajectories in X starting in the distant past converge (Arnold 1998; Rasmussen 2007; Kloeden and Rasmussen 2011; Carvalho et al. 2012). As we shall see later, such a global PBA might include two or more local attractors, which only attract trajectories from certain subsets of X. These concepts are clarified and discussed further in the present paper's appendix. When the equations or the forcing include stochastic processes, a PBA is called a random attractor. In the physical literature, Romeiras et al. (1990) introduced the somewhat vaguer concept of a snapshot attractor.

The concepts and methods of nonautonomous and random dynamical systems, including pullback attraction, were introduced into climate dynamics by Ghil et al. (2008) and Chekroun et al. (2011), and they were also pursued vigorously by T. Tél and his group (Bódai et al. 2011; Bódai and Tél 2012; Bódai et al. 2013). Several recent studies have explored the properties of PBAs for low-order climate models using ensemble simulations (Bódai et al. 2011, 2013; Bódai and Tél 2012; De Saedeleer et al. 2013; Pierini 2014a; Drótos et al. 2015).

Drótos et al. (2015) used the simple conceptual climate model of Lorenz (1984), forced by a periodic seasonal component and a linear decrease in the imposed equator-to-pole temperature difference. These authors argued that the PBAs—or snapshot attractors, using the simpler concept introduced by Romeiras et al. (1990)—and their natural probability distributions are the only tools with which mathematically sound statements can be made at a given point in time within a changing climate. Their claim was based on the finding that the time-dependent, chaotic attractor of the Lorenz (1984) model was independent of the initial states, or initial data (IDs) for short, within the parameter ranges and for the ensembles of IDs they considered. This claim appears to be fully justified for the Lorenz (1984) model, which seems to possess a unique global PBA in those parameter ranges.

The ensemble simulations of a periodically forced quasigeostrophic ocean model by Pierini (2014a) also provided evidence of ID independence in chaotic regimes, but dependence on the IDs did emerge for particular parameter ranges, for which chaotic basins of attraction coexist with nonchaotic basins; trajectories starting in the latter converge onto small subsets of the PBA. Thus, the fundamental problem of the dependence of the natural probability distribution of a changing climate on initial states needs further investigation.

In this paper, we carry out such an investigation. The four-variable quasigeostrophic model of the ocean's wind-driven, double-gyre circulation formulated by Pierini (2011) and used in the periodically forced simulations of Pierini (2014a) is studied here via ensemble simulations subject to a deterministic aperiodic forcing that mimics time dependence dominated by interdecadal climate variability. Two reference cases separated by a tipping point are considered: above the tipping point, large-amplitude relaxation oscillations shape the behavior of the autonomous system, whereas below it small-amplitude oscillations are dominant. In this second range the system is excitable, because an appropriate time-dependent forcing can excite the relaxation oscillations (e.g., Pikovsky and Kurths 1997; Pierini 2011, 2012). Various properties of these two reference cases are analyzed, such as the time of convergence from arbitrary IDs to PBAs and the sensitivity of the latter to forcing amplitude, as well as the dependence of the local attractors on the choice of the initial ensemble of states.

The paper is organized as follows. In section 2, the model is described and basic aspects of the autonomous system's solutions and of the two reference ensemble simulations under aperiodic forcing are discussed. In section 3, the time of convergence from arbitrary IDs to the PBAs is estimated. In section 4, the sensitivity of PBAs with respect to the forcing amplitude is investigated. Section 5 is devoted to the dependence of PBAs on the choice of the ensemble of IDs: chaotic and nonchaotic basins of attraction are analyzed in detail. In section 6, the main results are summarized and discussed, and an appendix provides the rigorous mathematical background.

2. Model description

a. Model formulation

The mathematical model used in this study was developed by Pierini (2011) to analyze fundamental dynamical features of the decadal variability in the Kuroshio Extension (Dijkstra and Ghil 2005, and references therein). This model is derived through projection of the governing equations onto an orthonormal basis and subsequent low-order truncation, following

the approach of Platzman (1960), Saltzman (1962), Lorenz (1963), and many others since, such as Lorenz (1982), Legras and Ghil (1985), Ghil and Childress (1987), Olbers (2001), and Crucifix (2012). S. Pierini and colleagues had already investigated this decadal variability with a relatively realistic primitive equation ocean model (Pierini 2006; Pierini et al. 2009; Pierini 2010, 2014b).

The model is derived via a severe truncation of the spectral representation of the evolution equation of potential vorticity in the quasigeostrophic, reduced-gravity approximation, in a rectangular domain. The Cartesian orthonormal basis onto which the streamfunction $\psi(\mathbf{x}, t)$ is projected is composed of two trigonometric functions in the zonal and two in the meridional direction; the zonal ones incorporate, moreover, the exponential factor proposed by Jiang et al. (1995) to account for westward intensification of midlatitude surface currents. Here $\mathbf{x}$ is the vector of horizontal coordinates and t is time.

The nonlinear coupled ordinary differential equations for the variables $\Psi_i(t)$, $i = 1, \ldots, 4$ are given by

$$\begin{aligned}
&\dot{\Psi}_1 + L_{11}\Psi_1 + L_{13}\Psi_3 + B_1(\Psi,\Psi) = W_1(t),\\
&\dot{\Psi}_2 + L_{22}\Psi_2 + L_{24}\Psi_4 + B_2(\Psi,\Psi) = W_2(t),\\
&\dot{\Psi}_3 + L_{33}\Psi_3 + L_{31}\Psi_1 + B_3(\Psi,\Psi) = W_3(t),\\
&\dot{\Psi}_4 + L_{44}\Psi_4 + L_{42}\Psi_2 + B_4(\Psi,\Psi) = W_4(t). \qquad (1)
\end{aligned}$$

Here Ψ denotes the vector of expansion coefficients $(\Psi_1, \Psi_2, \Psi_3, \Psi_4)$ of the streamfunction, $\mathbf{W}$ will be used as the vector of forcing terms (W_1, W_2, W_3, W_4), and the bilinear terms B_i are given by

$$\begin{aligned}
B_1(\Psi,\Psi) &= 2J_{112}\Psi_1\Psi_2 + 2J_{114}\Psi_1\Psi_4 + 2J_{123}\Psi_2\Psi_3 + 2J_{134}\Psi_3\Psi_4,\\
B_2(\Psi,\Psi) &= J_{211}\Psi_1^2 + J_{222}\Psi_2^2 + J_{233}\Psi_3^2 + J_{244}\Psi_4^2 + 2J_{213}\Psi_1\Psi_3 + 2J_{224}\Psi_2\Psi_4,\\
B_3(\Psi,\Psi) &= 2J_{312}\Psi_1\Psi_2 + 2J_{314}\Psi_1\Psi_4 + 2J_{323}\Psi_2\Psi_3 + 2J_{334}\Psi_3\Psi_4,\\
B_4(\Psi,\Psi) &= J_{411}\Psi_1^2 + J_{422}\Psi_2^2 + J_{433}\Psi_3^2 + J_{444}\Psi_4^2 + 2J_{413}\Psi_1\Psi_3 + 2J_{424}\Psi_2\Psi_4. \qquad (2)
\end{aligned}$$

The analytical expressions of the Jacobian coefficients J_{ijk}, the linear ones L_{ij}, and the forcing terms W_i were derived by Pierini (2011); moreover, all the parameter values used here are the same as adopted in that study and in Pierini (2014a). Pierini (2012) used the model governed by Eqs. (1) and (2) to systematically analyze abrupt climate changes seen as noise-induced transitions in excitable systems, while S. Vannitsem and colleagues (Vannitsem 2014a,b; Vannitsem and De Cruz 2014) used it to represent the ocean component in their low-order ocean–atmosphere coupled models. Pierini (2014a) applied periodic forcing to model (1) and explored the PBAs of the forced system. The present study can thus be seen as the extension of the latter study to an aperiodic forcing case.

In this study, the forcing $\mathbf{W}(\mathbf{x}, t)$ is defined as

$$\mathbf{W}(\mathbf{x}, t) = \gamma[1 + \varepsilon f(t)]\mathbf{w}(\mathbf{x}), \quad f(t) = F_{T_f}[\zeta(t)]. \qquad (3)$$

Here $\mathbf{w}(\mathbf{x})$ is the double-gyre wind stress curl used in Pierini (2011), with γ its dimensionless intensity, while $\zeta(t)$ is a fixed realization of an Ornstein–Uhlenbeck process, normalized to have unit variance and an autocorrelation time T_a. This fixed realization is smoothed with the sliding window F_{T_f} of width T_f, and the resulting aperiodic forcing $f(t)$ is weighted by the dimensionless parameter ε.

b. Model behavior

In the autonomous case, there is no t dependence and we let $\varepsilon = 0$. The bifurcation diagram in this case is plotted in Fig. 1a. This diagram is obtained by forward integration of the model, starting from vanishing initial data and dropping a sufficiently long initial segment of the trajectories. The time needed for the trajectories to land on the model's attractor is discussed in the appendix.

The value $\gamma = 0.96$ corresponds to the blue limit cycle shown in Figs. 1b and 1c, in the planes (Ψ_1, Ψ_3) and (Ψ_2, Ψ_4), respectively. This limit cycle lies above the supercritical Hopf bifurcation that occurs at $\gamma \simeq 0.348$ (cf. Pierini 2011) and resembles a linear, harmonic oscillation.

The value $\gamma = 1.1$, however, corresponds to a much larger and more complex limit cycle, plotted in red in Figs. 1b and 1c. This limit cycle is associated with a relaxation oscillation that can be excited by an appropriate noise or deterministic time-dependent forcing when the system lies below a homoclinic bifurcation (e.g., Simonnet et al. 2005; Pierini 2011). The sudden growth in the size and complexity of the closed, periodic trajectory at $\gamma = 1.0$ corresponds to such a global bifurcation.

Pierini (2011, 2012, 2014a) did, in fact, study already the present model in the presence of both stochastic and deterministically periodic forcing, and found that such a homoclinic bifurcation does occur in it and that this bifurcation gives rise to what is currently termed a tipping

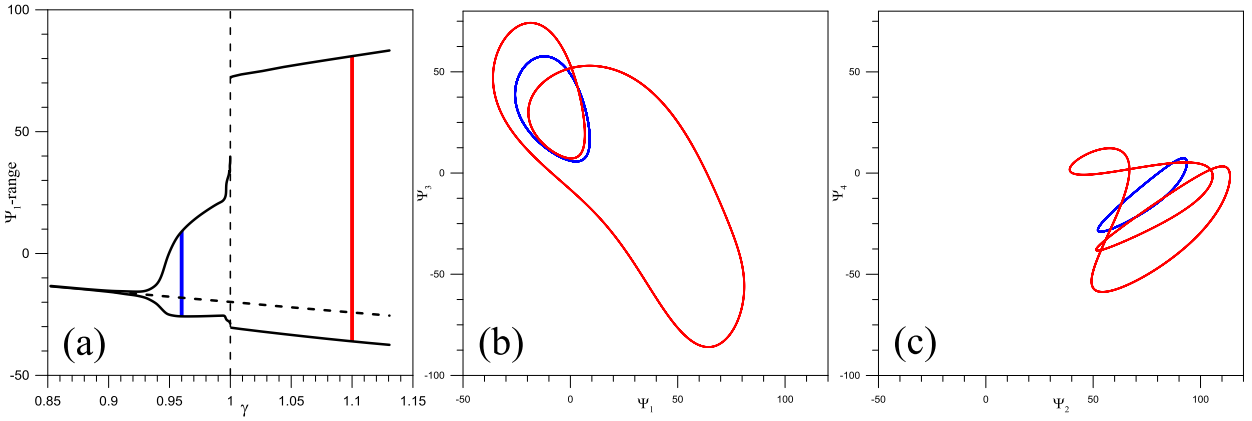

FIG. 1. Bifurcation diagram of our idealized ocean model (1) in the autonomous case, i.e., with $\varepsilon = 0$ in Eq. (3). (a) The range of the variable Ψ_1 is plotted vs the wind stress intensity γ. (b),(c) The limit cycles corresponding to the blue and red vertical segments in (a) are shown here projected onto the planes (Ψ_1, Ψ_3) and (Ψ_2, Ψ_4), respectively.

point by the climate community (e.g., Lenton et al. 2008). Such a dynamical mechanism is a typical paradigm of abrupt climate change associated with an intrinsically nonlinear mode of variability (Lorenz 1963; Ghil and Childress 1987; Crucifix 2012), and it is sometimes called coherence resonance (Pikovsky and Kurths 1997). When coherence resonance does occur, the system displays strong dependence on forcing amplitude, as we will see in section 4.

In the nonautonomous case, $\varepsilon \neq 0$ in Eq. (3), and we use the fixed aperiodic forcing $f(t)$ obtained with autocorrelation time T_a and a sliding window F_{T_f} of width T_f. Figure 2a shows a realization with $T_a = T_f = 15$ yr and $\varepsilon = 0.2$. This choice provides an idealized aperiodic forcing that mimics North Pacific multidecadal variability (Chao et al. 2000; Chang et al. 2015) for the minimal representation of the Kuroshio Extension provided by (1). On the other hand, the relaxation

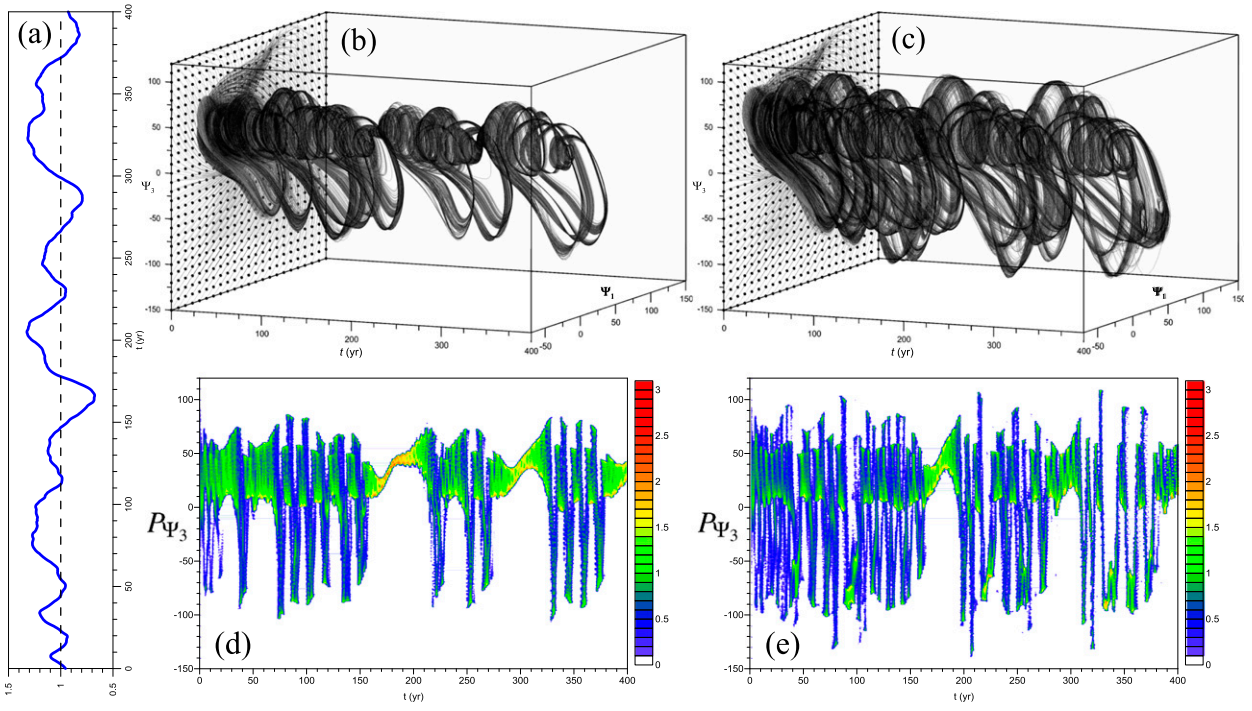

FIG. 2. Ensemble behavior of forced solutions of the double-gyre ocean model. (a) Time dependence of the total forcing $1 + \varepsilon f(t)$, for $\varepsilon = 0.2$. (b),(c) Evolution of 644 initial states emanating from the subset Γ in the (Ψ_1, Ψ_3) plane for (b) $\gamma = 0.96$ and (c) $\gamma = 1.1$. (d),(e) Corresponding time series of P_{Ψ_3}. The set Γ is given by $\{-70 \leq \Psi_1 \leq 150\} \times \{-150 \leq \Psi_3 \leq 120\}$.

oscillations of the autonomous model display decadal variability as well, in agreement with the oceanic phenomenon that inspired this simple model. The dimensional time variable used throughout this paper refers to this multidecadal interpretation, although the present model's properties are likely to be shared by a wide class of systems of climate relevance.

Apart from this oceanographic interpretation, the forcing in Eq. (3) extends the analysis of Pierini (2014a) from purely periodic to deterministically aperiodic. This choice disrupts the cyclostationarity and cycloergodicity properties of PBAs and makes the forced model's behavior more realistic.

The evolution of the model solutions subject to the forcing of Fig. 2a is shown in Figs. 2b and 2c for two reference cases, $\gamma = 0.96$ and $\gamma = 1.1$, respectively; the solutions of the corresponding autonomous system (i.e., with $\varepsilon = 0$) are plotted in Figs. 1b and 1c. In the present figure, N trajectories $\Psi_k(t)$ emanate from N IDs uniformly distributed at time $t_0 = 0$ on a reference subset Γ of the (Ψ_1, Ψ_3) plane, which is shown in Figs. 2b and 2c here, while the (Ψ_2, Ψ_4) coordinates of the initial states (not shown) are chosen the same way as in Pierini (2014a).

Figures 2b and 2c provide a first representation of the sets that approximate the corresponding PBAs; the small number of trajectories is in fact chosen for the sake of graphical clarity. The correct identification and characterization of the PBAs requires, however, an analysis of the PDFs that evolve along the trajectories and of the convergence to the appropriate invariant time-dependent sets. This convergence is investigated in the next section.

3. Convergence to PBAs

As mentioned in the introduction, PBAs are the extension of the attractors of dissipative autonomous dynamical systems to the nonautonomous case. When time-dependent forcing is present, the trajectories originating from the set $\Gamma = (-70 \le \Psi_1 \le 150, -150 \le \Psi_3 \le 120)$ of IDs at time τ tend to a subset $\mathscr{A}(\tau, t)$ of phase space at time $t > \tau$, but while $\mathscr{A}(t)$ depends on τ in general, in the limit of $\tau \to -\infty$ this dependence vanishes.

The limit $\tau \to -\infty$ is the pullback limit and it provides the natural generalization of the forward asymptotics associated with autonomous systems (Arnold 1998; Rasmussen 2007; Kloeden and Rasmussen 2011; Carvalho et al. 2012; Ghil et al. 2008; Chekroun et al. 2011); see the appendix herein. In practical terms, though, a question arises: How large should $|\tau|$ be for $\mathscr{A}(\tau, t)$ to be virtually independent of τ?

An effective way to answer this question is to compute the PDF of the localization of the trajectories that emanate from Γ. To obtain a function that provides a clear graphical representation of the invariant measure on the attracting set, the following parameter is computed:

$$P_{\Psi_3} = \log_{10}(1000 p_{\Psi_3}), \tag{4}$$

where $p_{\Psi_3}(t)$ is the PDF of localization of the Ψ_3 variable using the $N = 644$ trajectories shown in Figs. 2b and 2c. To make p_{Ψ_3} independent of the length $T_{\rm tot} = t_{\rm fin} - \tau$ of the signal (this is important to make the panels of Fig. 3 comparable; see below), $T_{\rm tot}$ is decomposed into n cells and p_{Ψ_3} is scaled in such a way that its integral over each cell equals 1. In our case $T_{\rm tot} = 400$ yr and $n = 300$.

In Figs. 2d and 2e, we plot $P_{\Psi_3}(t)$ for the trajectories shown in Figs. 2b and 2c, respectively. The variability in P_{Ψ_3} induced by the forcing of Fig. 2a is impressive when compared with Figs. 4a and 4f, which are discussed in section 4 and were obtained with $\varepsilon = 0$. Of particular interest is the remarkable reduction of the range of variability of P_{Ψ_3} found at $t \simeq 170 - 185$ yr and at $t \simeq 295 - 310$ yr. This variability reduction is most evident in the case with $\gamma < 1$ (Fig. 2d) and it corresponds to a partial synchronization of the trajectories. As we will see in section 4, both synchronization episodes occur when the total forcing $\gamma[1 + \varepsilon f(t)]$ decreases well below unity.

To estimate the rate of converge to the PBA, five cases are considered in Fig. 3, for both $\gamma = 0.96$ and $\gamma = 1.1$. The trajectories emanate from the same distribution of IDs but at the different initial times $\tau = t_{01}, \ldots, t_{05} = 200, 150, 100, 50, 0$ yr. Comparison of $P_{\Psi_3}(t; t_{0i})$ with $P_{\Psi_3}(t; t_{0i+1})$ shows that the two distributions coincide when t in the former is greater than $t \simeq t_{0i} + 15$ yr. We can therefore conclude that the set to which the trajectories converge approximates well the PBA after roughly 15 yr from the beginning of the integration, and that this important result holds at any time during the nonstationary process.

4. Sensitivity of PBAs to the amplitude of the forcing

Model robustness is important in making any inferences about the role of time-dependent forcing (Ghil 2015, and references therein). We thus proceed to analyze in this section the sensitivity of the present model's PBAs with respect to the amplitude ε of the time-dependent component of the forcing, while in the next section dependence on IDs will be analyzed.

Figure 4 shows the dependence of $P_{\Psi_3}(t)$ on ε, with this amplitude increasing from $\varepsilon = 0$ (i.e., the autonomous case) in the top two panels to $\varepsilon = 0.2$ (the value

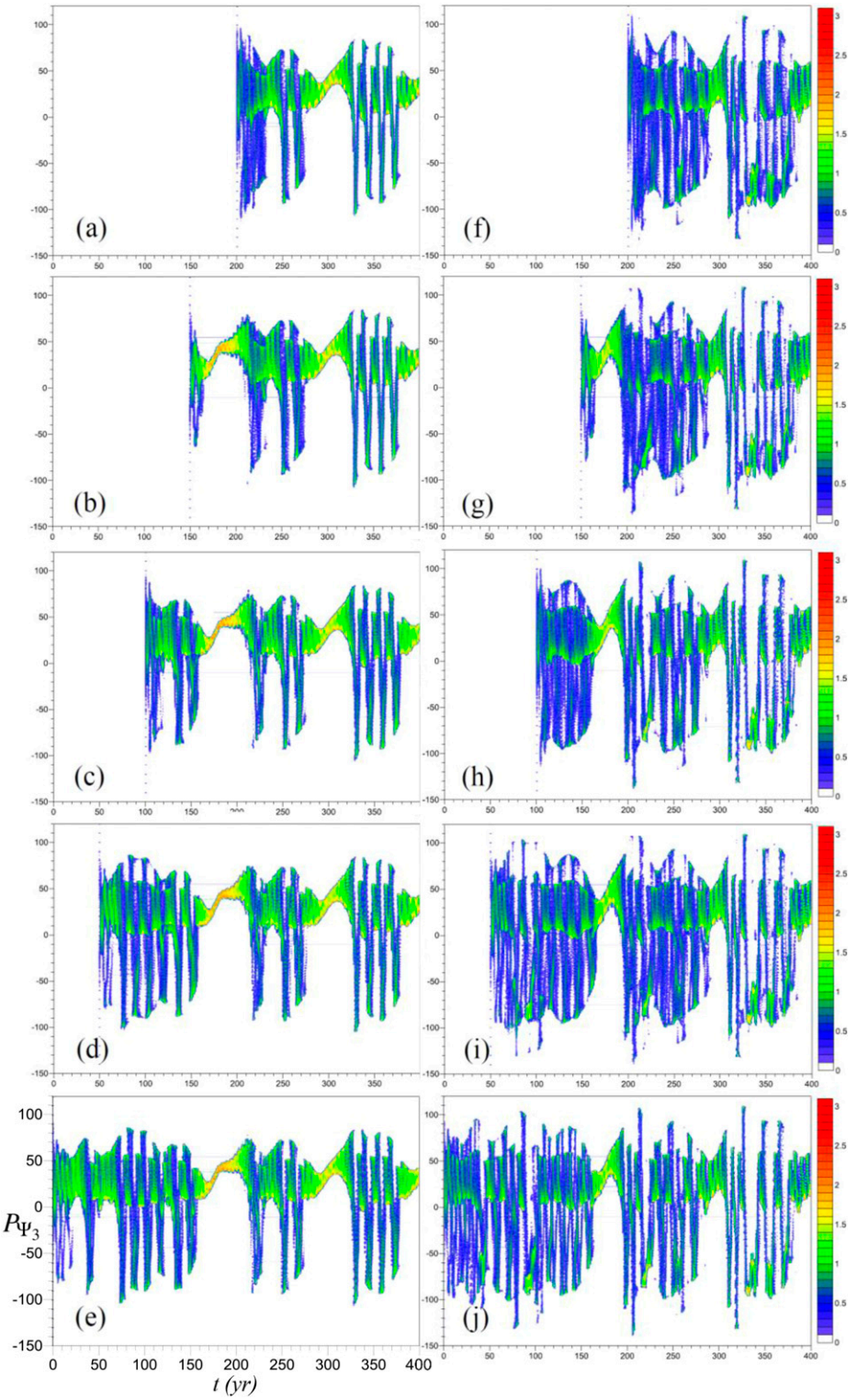

FIG. 3. Evolution in time of P_{Ψ_3} as a function of the initial time t_{init}, for (left) $\gamma = 0.96$ and (right) $\gamma = 1.1$, for different initial times but with the same distribution of IDs.

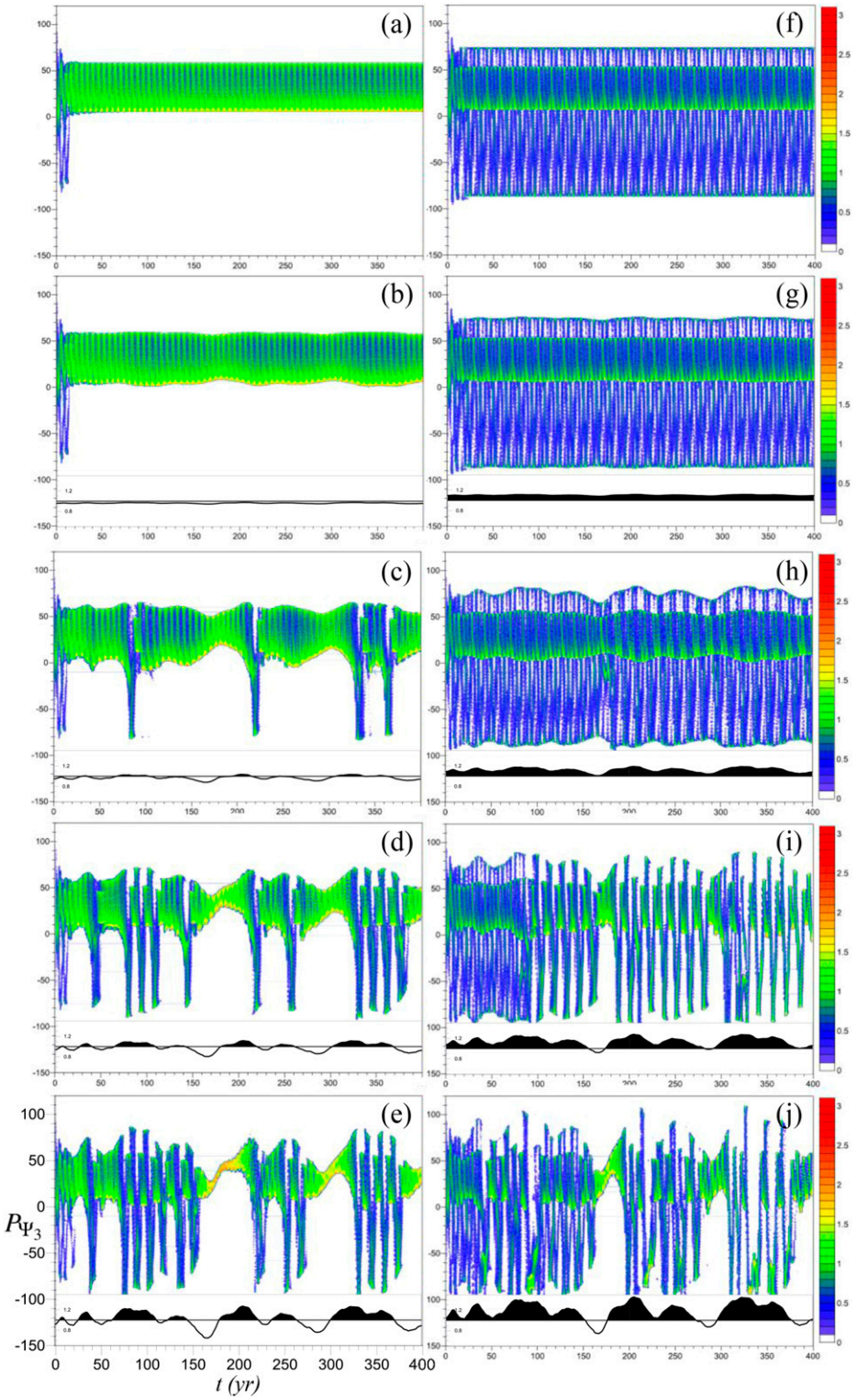

FIG. 4. Evolution in time of P_{Ψ_3} as a function of the amplitude ε of the time-dependent part of the forcing, $\varepsilon f(t)$, for (left) $\gamma = 0.96$ and (right) $\gamma = 1.1$. The amplitudes are (a),(f) $\varepsilon = 0$, (b),(g) $\varepsilon = 0.01$, (c),(h) $\varepsilon = 0.05$, (d),(i) $\varepsilon = 0.1$, and (e),(j) $\varepsilon = 0.2$. The total forcing amplitude $\overline{\gamma}(t) = \gamma[1 + \varepsilon f(t)]$ is reported at the bottom of each panel (the black areas correspond to $\overline{\gamma} > 1$).

used in Fig. 2) in the bottom two panels, while the overall intensity γ of the total wind stress equals 0.96 in the left column and 1.1 in the right column, as in Figs. 2 and 3. The PBAs corresponding to the blue and red limit cycles visible in Fig. 1b are shown here in Figs. 4a and 4f. It is interesting to notice that, for $\varepsilon = 0$, any point of Γ evolves toward the same limit cycle, while the phase of each orbit on its limit cycle does depend on the IDs. Note that the limit cycles in Figs. 1b and 1c were obtained, like the bifurcation diagram in Fig. 1a, from vanishing initial data, $\{\Psi_i(0) = 0: i = 1, 2, 3, 4\}$.

Inspecting the panels of the left column, which correspond to $\gamma < 1$, from top to bottom, shows a dramatic transition from the small limit cycles, in the top two rows, to the highly variable ones of the bottom two rows. To better understand this behavior, the total time-dependent forcing amplitude $\overline{\gamma} = \gamma[1 + \varepsilon f(t)]$ is plotted at the bottom of each panel. Each transition from small- to large-amplitude oscillations is preceded by an increase of $\overline{\gamma}$ above the critical level $\overline{\gamma} = 1$; consider, for instance, the one already noticed in Figs. 2d and 4e. More generally, coherence resonance is activated when $\overline{\gamma} > 1$, provided this has occurred at least 10–30 yr in advance; note that even very small positive excursions above $\overline{\gamma} = 1$ yield the same behavior, as shown for example in Fig. 4c.

This result agrees with Pierini (2012), who noticed that model (1), when subjected to stochastic forcing, behaves approximately like an adiabatically changing autonomous dynamical system, as far as coherence resonance is concerned. Likewise, when $\overline{\gamma}$ decreases well below unity, the system tends to produce small-amplitude limit cycles, according to the bifurcation diagram of Fig. 1a: this corresponds to the synchronization events already discussed.

The same behavior is found for $\gamma > 1$, in the right column of Fig. 4, but now the relaxation oscillations are typically present, since they are self-sustained and since $\overline{\gamma} > 1$ is the norm. The consequence of the fluctuations of $\overline{\gamma}$ on $P_{\Psi_3}(t)$ can again be easily interpreted by taking into account the diagram of Fig. 1a. Three synchronization events are present for $\varepsilon = 0.2$ (Fig. 4j), after intervals during which $\overline{\gamma} < 1$. In general, if $\gamma > 1$, the changes in the PBA are less dramatic.

5. PBA dependence on the choice of initial ensemble

In section 3, we have investigated the evolution of the same set of IDs starting from different initial times τ; here we study the evolution of different initial states starting from the same initial time $\tau = 0$. This second analysis is fundamental in a climate perspective, as it concerns the dynamical origin of the PBAs and of the invariant measures supported on them, as well as the dependence of predictability on IDs.

In the periodic-forcing case, Pierini (2014a) provided numerical evidence that the present ocean model's PBA can be obtained from any set of IDs, provided its evolution is chaotic; see Figs. 3e and 3f therein. Drótos et al. (2015) have recently stressed that the chaotic PBAs of the Lorenz (1984) atmospheric model are independent of IDs and have suggested that this is likely to be the typical situation in climate models.

PBA dependence on IDs may, however, be more complex. In his systematic study of the present model's PBAs as a function of the forcing period, Pierini (2014a) identified periods for which a chaotic basin of attraction—which converges onto the global PBA—coexists with nonchaotic basins. Thus, for example, a chaotic basin can coexist with another basin whose phase-space flow converges onto a single periodic trajectory lying on the global PBA; see, for example Figs. 6a–c of Pierini (2014a). It is therefore natural to investigate whether a similar behavior may be present also in the aperiodic-forcing case studied in the present paper. In the following, we use two complementary mathematical tools to explore this possibility.

a. Finite-time Lyapunov exponents

The typical approach to the investigation of chaotic versus nonchaotic behavior is to evaluate the finite-time Lyapunov exponents (FTLEs) of the system (Nese 1989). FTLEs have been widely used in physical oceanography to help identify localized coherent structures and material surfaces (Haller 2001; D'Ovidio et al. 2009).

If two nearby points—whose distance according to Eulerian metrics in phase space is δ_0 at time $t = 0$ and δ_t at time t—diverge exponentially in time, the Lyapunov exponent

$$\lambda_t = \frac{1}{t} \ln \frac{\delta_t}{\delta_0} \tag{5}$$

is independent of t and it is positive; if, on the contrary, the trajectories converge exponentially, then λ_t is still independent of t and it is negative. In the presence of a bound on the region of phase space occupied by all possible model trajectories, divergence of trajectories indicates that the behavior is chaotic (e.g., Ghil and Childress 1987).

To test whether chaotic behavior may coexist with nonchaotic trajectories, we computed maps of $\lambda_t = \lambda(\Psi_1, \Psi_3, t)$ for trajectories that originate from a homogeneous distribution of δ_0 at times $t = 20$, 40, and

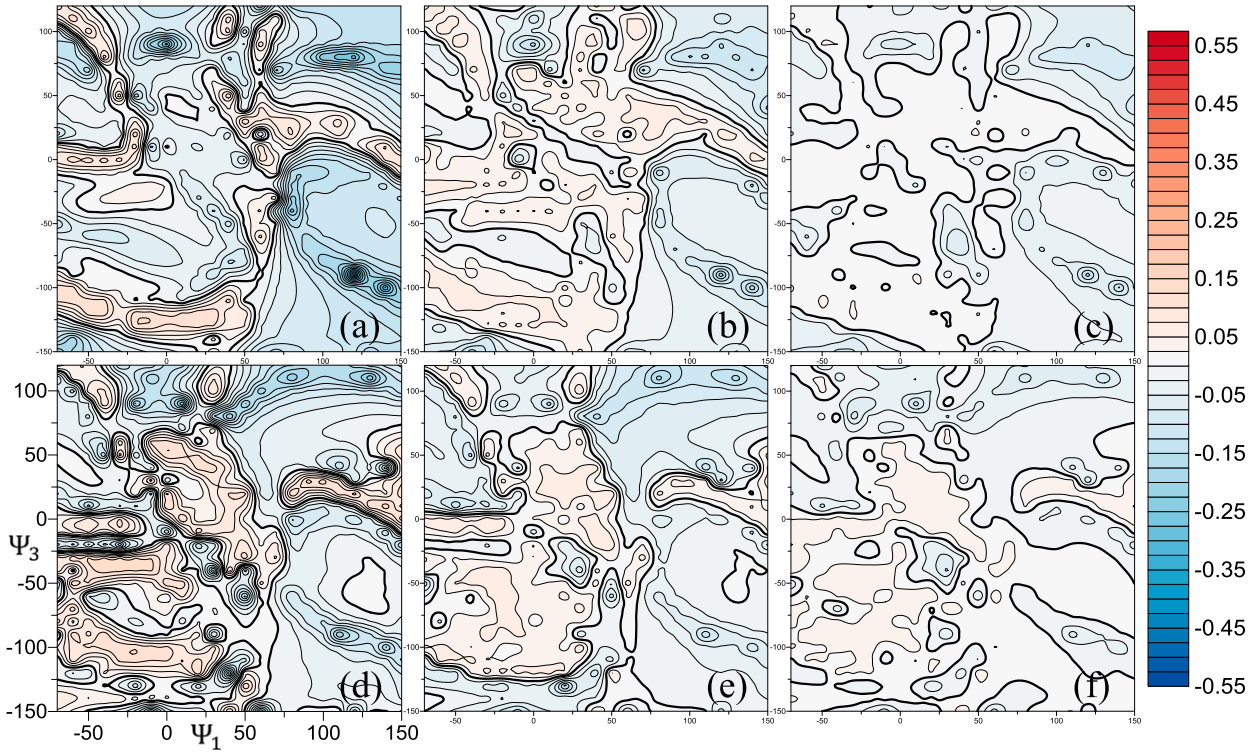

FIG. 5. Maps of FTLEs for the present model. Maps of $\lambda(\Psi_1, \Psi_3, t)$ at (a),(d) $t = 20$ yr, (b),(e) $t = 40$ yr, and (c),(f) $t = 60$ yr, for (top) $\gamma = 0.96$ and (bottom) $\gamma = 1.1$. In the color bars to the right, warm colors indicate instability, i.e., $\lambda_t > 0$, and cool colors the opposite, while heavy black lines in the panels correspond to $\lambda = 0$.

60 yr. These maps are plotted in Fig. 5 for both $\gamma = 0.96$ and $\gamma = 1.1$.

The first thing to note in all six panels is the existence of extensive regions in which $\lambda_t > 0$ that coexist with regions where $\lambda_t < 0$, so the chaotic nature of the flow is far from being independent on IDs for the model (1), subject to the aperiodic forcing of Fig. 2a. Another notable feature is that λ_t exhibits strong time dependence, for both $\gamma < 1$ (upper panels) and $\gamma > 1$ (lower panels).

The remarkable decrease of the range of λ_t as t increases from $t = 20$ yr to $t = 60$ yr, both in Figs. 5a–c and Figs. 5d–f, is to be expected, due to the saturation of the exponential behavior, but the spatial distribution depends strongly on time as well. This dependence clearly indicates that complex temporal behavior lies behind these maps, which cannot, therefore, provide an unambiguous indication of the flow's chaoticity depending on (Ψ_1, Ψ_3). (Such complexities are further discussed in connection with Fig. 8 below.)

b. *Mean normalized distance*

A more robust identification of chaotic and nonchaotic regions within the set Γ of initial states can be obtained by introducing and evaluating the metric σ, defined by

$$\sigma(\Psi_1, \Psi_3) = \langle \delta_n \rangle_{T_{\rm tot}}, \tag{6}$$

where the normalized distance δ_n, given by $\delta_n = \delta_t/\delta_0$, is averaged over the whole forward time integration $T_{\rm tot} = t_{\rm fin} - t_{\rm init}$ of the available trajectories. The maps of σ in Fig. 6 reveal large chaotic regions where $\delta_n \gg 1$ on average (warm colors) but also nonchaotic regions where $\sigma \leq 1$ (blue) and thus initially close trajectories do remain close on average.

To check the character of the two types of evolution, we plot in Fig. 7 many trajectories that leave two small subsets of Γ for which $\sigma \gg 1$—namely the sets A and C in Fig. 6, for $\gamma = 0.96$ and $\gamma = 1.1$, respectively—to compare with those that leave the sets B and D of Fig. 6, for which $\sigma \leq 1$.

Figures 7a and 7c confirm the extreme sensitivity to IDs that lie in boxes A and C: a comparison of these two panels with Figs. 2b and 2c, respectively, shows that the attracting sets to which trajectories started in A and B converge are dense in the PBAs obtained by starting from the whole Γ. The corresponding PDFs, as represented by P_{Ψ_3} (not shown) coincide in fact with those of Figs. 2d and 2e and the same result is obtained by starting from any small region of Γ for which $\sigma \gg 1$. Figures 7b and 7d also confirm that the trajectories leaving from boxes B and D

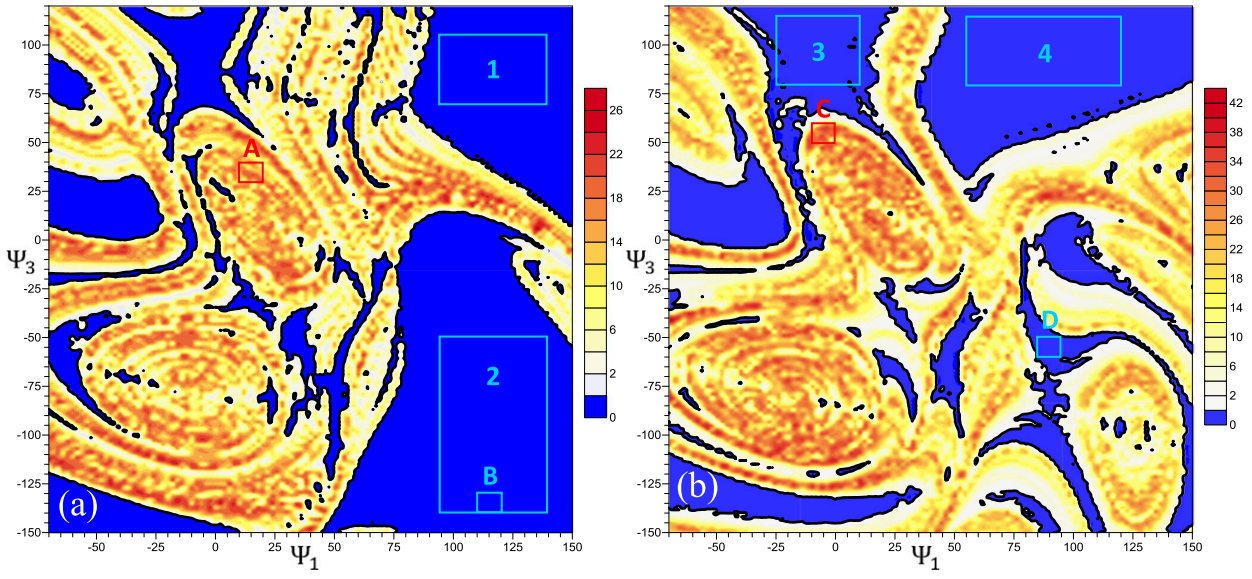

FIG. 6. Mean normalized distance $\sigma(\Psi_1, \Psi_3)$ for 15 000 trajectories starting in the initial set Γ: (a) $\gamma = 0.96$ and (b) $\gamma = 1.1$. The boxes A–D and 1–4 indicate subdomains of Γ from which IDs are taken for our analysis (see text).

converge to time-dependent sets in the (Ψ_1, Ψ_3) plane whose measure is much smaller than that of either B or D.

c. *Discussion*

It is worth exploring in greater detail the evolution of some of the trajectories plotted in Fig. 7. We display in the top graphs of Figs. 8a–d the Ψ_3 time series of two initially nearby trajectories selected among those of Figs. 7a–d, respectively; each pair of trajectories has lines, one in blue and one in red, both drawn from the same panel of Fig. 7. The corresponding normalized distances $\delta_n(t)$ are shown in the bottom graphs of Figs. 8a–d marked with a prime.

In the chaotic cases, represented by both graphs in Figs. 8a, and 8c, the values of $\delta_n(t)$ range from $\delta_n(t) \simeq 1$ to $\delta_n(t) \gg 1$, up to order 10^2; the former very small values occur over the same time intervals—already apparent in Figs. 2b′ and 2c′—in which synchronization sets in. In the nonchaotic cases, like those of Figs. 8b, 8d, the values of δ_n lie typically below unity, although an initial divergence is noticeable in Fig. 8d′; this slow divergence may be due to a transient growth of polynomial rather than exponential nature.

Inspection of the bottom graphs in Figs. 8a–d confirms the validity of the mean normalized distance σ of Eq. (6) as a sharper diagnostic tool than the FTLEs. Longer integrations (not shown) simply extend in time the ensemble of trajectories shown in Figs. 7a and 7b, but the chaotic versus nonchaotic character of the trajectories—as diagnosed by σ—is preserved.

To further analyze the structure of the model's PBAs, the intersection of many trajectories with the (Ψ_1, Ψ_3) plane at a reference time $t = 330$ yr is shown in Figs. 9a and 9b for $\gamma = 0.96$ and $\gamma = 1.1$, respectively. The gray dots in both panels arise from 15 000 IDs evenly distributed in Γ and are associated with the filamentary patterns that characterize chaotic attractors (e.g., Chekroun et al. 2011; Drótos et al. 2015).

The red dots arise from the small boxes A and C that are located in the chaotic regions of Figs. 6a and 6b, respectively. These red dots, too, are distributed all over the corresponding attractors in the two panels, as expected from the previous analysis; in fact, only the 420 red dots that correspond to the trajectories of Figs. 7a and 7c have been plotted here, to avoid complete overlapping with the gray dots.

On the contrary, the cyan dots that arise from the large nonchaotic boxes 1, 2, 3, and 4 of Figs. 6a and 6b converge onto small subsets of the PBAs. This convergence onto a smaller-dimensional set is very similar to what Pierini (2014a) found for some forcing periods that yielded periodic PBAs; for example, see Figs. 6a–c therein.

For $\gamma > 1$ in Fig. 9b, the similarity with the result of Pierini (2014a) is striking because all the trajectories originating from boxes 3 and 4 of Fig. 6b converge toward two distinct points. It is worth noting that the blue boxes 3 and 4 of Fig. 6b are separated by a chaotic ridge that apparently acts as a barrier separating two distinct basins of attraction, each converging to a single point. In this case the asymptotic evolution is independent of

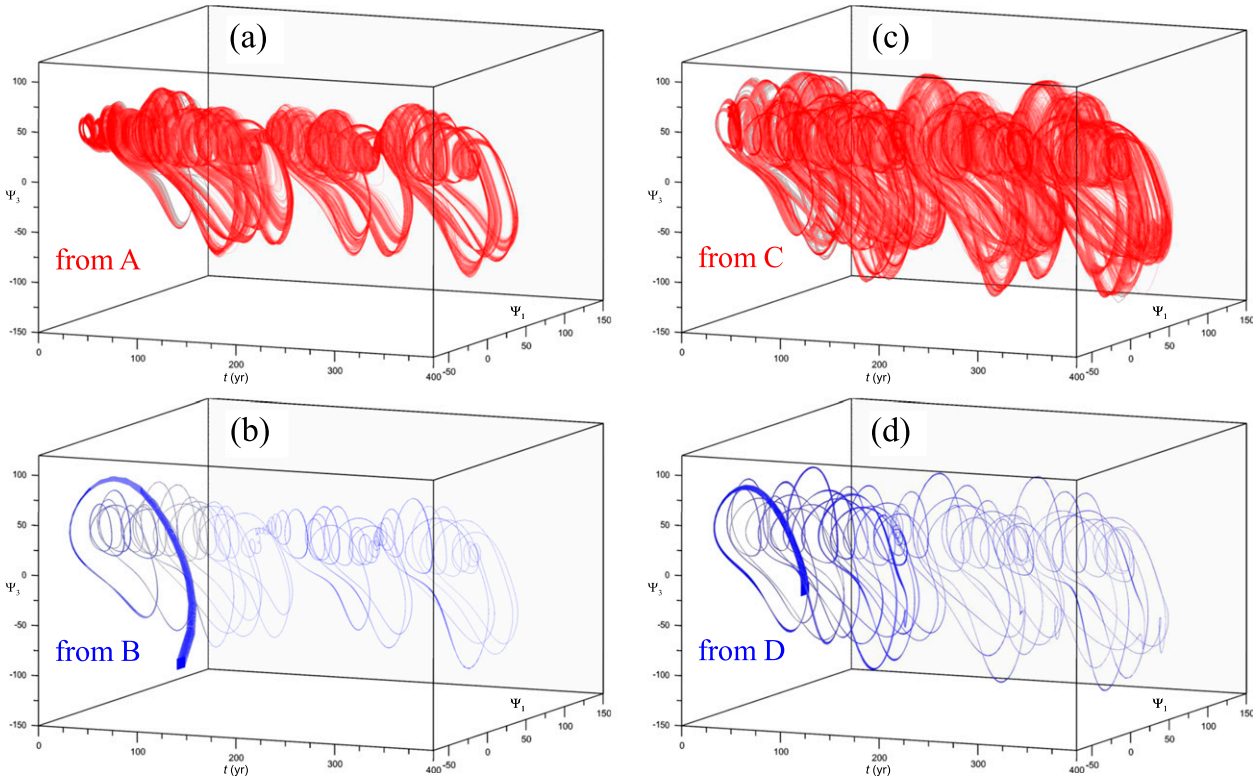

FIG. 7. Evolution of ensembles of 420 trajectories each that emanate from small subsets of Γ: (a),(b) $\gamma = 0.96$ and IDs in boxes A and B of Fig. 6a, respectively, and (c),(d) $\gamma = 1.1$ and IDs in boxes C and D of Fig. 6b, respectively.

initial data. On the other hand, for $\gamma < 1$ (Fig. 9a) the attracting cyan sets are small segments, so the evolution of the nonchaotic trajectories does depend, although very weakly, on IDs.

Graphs like those of Fig. 9 cannot provide quantitative information on the probability of localization of trajectories on the model's global PBA. Such information can be obtained, though, from the three-dimensional PDFs plotted in Fig. 10.

For the subcritical case $\gamma < 1$ in the left column of the figure, the distribution is highly inhomogeneous and concentrates in two areas labeled 1 and 2 in Fig. 10a; these concentrations extend over very small portions of the filament and result from large contributions of both chaotic (Fig. 10c) and nonchaotic (Fig. 10e) trajectories, with a larger contribution from the latter. In the supercritical case $\gamma > 1$ (right column), the same situation holds, with two peaks contained in the small area labeled 3.

In summary, in the small regions of phase space in which the invariant sample measure on our model's global PBA peaks in a filamentary pattern, both chaotic and nonchaotic trajectories coexist. The PDF peaks in Figs. 10a and 10b are clearly an indication of enhanced overall predictability, and recall those observed in Figs. 6 and 7 of Chekroun et al. (2011) for a highly idealized model of El Niño–Southern Oscillation with seasonal forcing.

6. Summary and conclusions

In this study, a low-order quasigeostrophic model of the wind-driven ocean circulation has been used as a prototype of an unstable, nonlinear, nonautonomous dynamical system of climatic relevance. We have studied this double-gyre model's PBAs (i.e., those time-dependent invariant sets that attract all trajectories initialized in the remote past) along with the invariant sample measures that live on these sets. PBAs (Arnold 1998; Ghil et al. 2008; Chekroun et al. 2011) and their close cousins, snapshot attractors (Romeiras et al. 1990; Bódai et al. 2011, 2013; Bódai and Tél 2012; Drótos et al. 2015), have only recently been recognized as the natural tools for investigating basic features of a changing nonequilibrium climate, and the theory of nonautonomous dynamical systems as the proper mathematical framework for such investigations.

We chose here an aperiodic forcing dominated by interdecadal variability to mimic the effects of multidecadal climate changes (Chang et al. 2015) on the

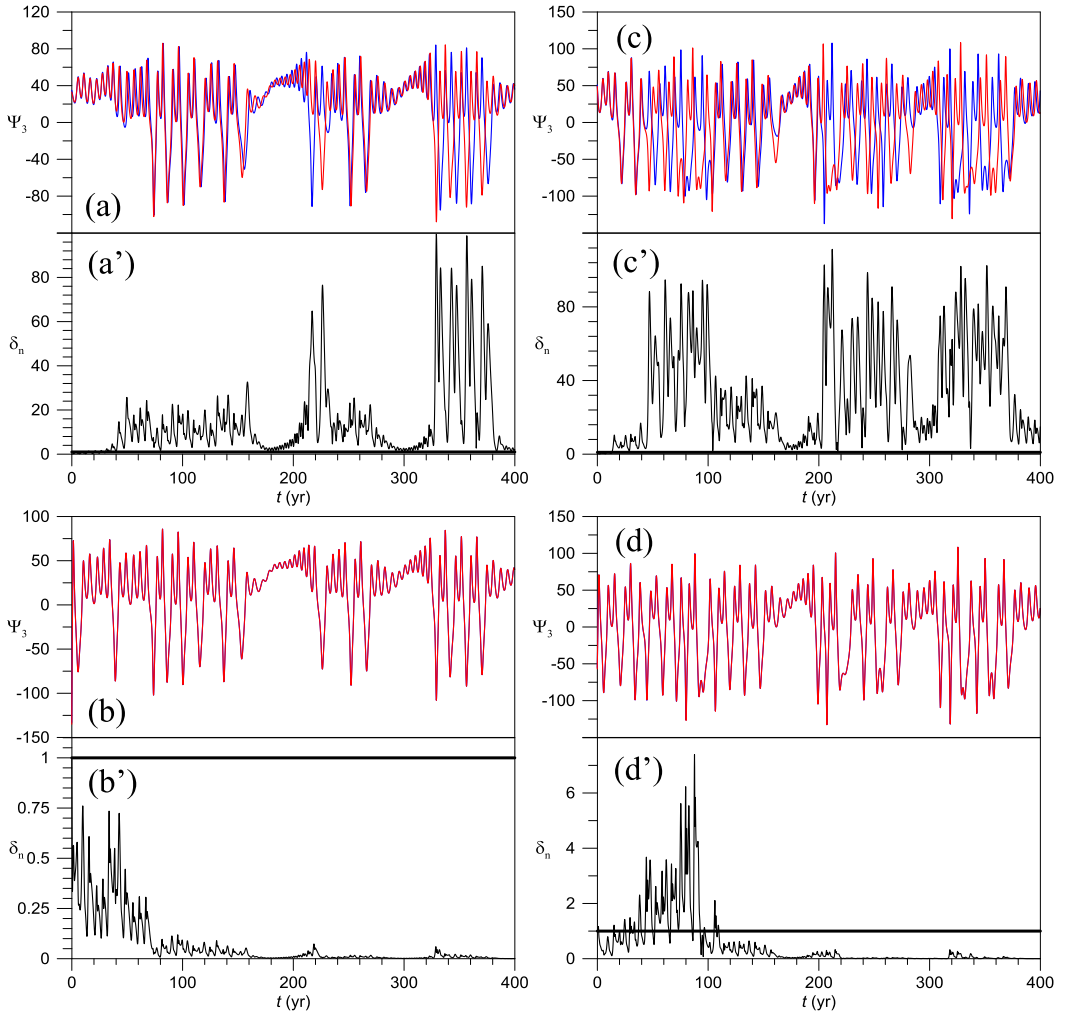

FIG. 8. Superposition of two time series of $\Psi_3(t)$ starting from nearby IDs in Γ. The initial points for $\gamma = 0.96$ are (a) (16, 36) and (b) (112, −132), while for $\gamma = 1.1$ they are (c) (−9, 51) and (d) (95, −55). The lower graphs in (a)–(d) marked with a prime are the corresponding normalized distances $\delta_n(t)$. The two nearby trajectories of (a)–(d) are included in those of Figs. 7a–d, respectively. The horizontal black lines mark the value $\delta_n = 1$.

midlatitude double-gyre circulation; see section 2. The present study generalizes therewith a set of results previously obtained in the presence of periodic forcing (Pierini 2014a). We recall that, in the absence of time-dependent forcing [i.e., when $\varepsilon = 0$ in Eq. (3)], a tipping point at $\gamma = 1$ separates small-amplitude, nearly harmonic oscillations from large-amplitude relaxation oscillations.

In section 3, the convergence of ensembles of trajectories to PBAs was assessed in order to estimate the time required to identify the PBAs. To do so, we considered—in addition to projections of the trajectories from the full, four-dimensional phase space onto a plane spanned by the Ψ_1 and Ψ_3 variables—the suitably scaled, time-dependent statistic $P_{\Psi_3}(t)$; see Eq. (4) and Fig. 2. A key result of this section is that a period of about 15 years suffices for trajectories to converge to the PBA.

The sensitivity of PBAs with respect to the amplitude ε of the time-dependent portion of the forcing was studied in section 4. Below the tipping point $\gamma = 1$, the range of variability within the PBA increases dramatically as ε increases, and so does the intermittency; see left column of Fig. 4. For $\gamma > 1$, the changes in both range and intermittency are less striking (cf. right column of Fig. 4). The difference in behavior is clearly associated with the solutions of the autonomous system: a small-amplitude limit cycle for $\gamma < 1$ versus a higher-amplitude, more complex and self-sustained relaxation oscillation for $\gamma > 1$.

Finally, the dependence of the attracting sets on the choice of the ensemble of initial states is investigated in

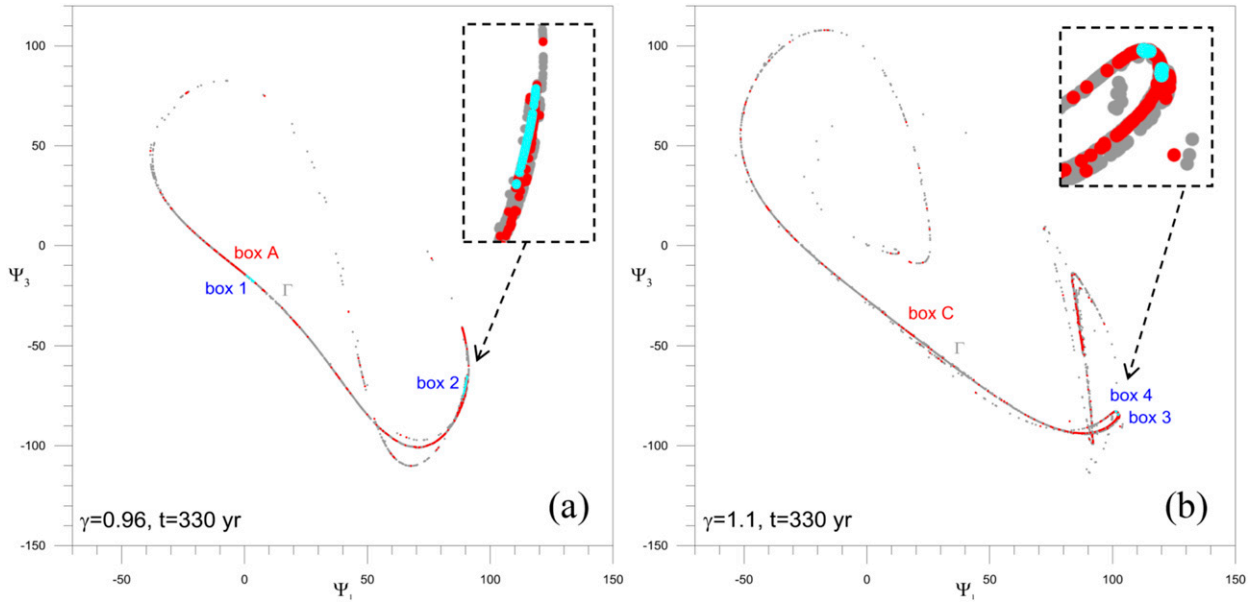

FIG. 9. (a) Intersection with the (Ψ_1, Ψ_3) plane at $t = 330$ yr of 15 000 trajectories (gray dots) emanating from the whole set Γ, and from boxes 1 and 2 (cyan dots, insets) and A (red dots) of Fig. 6a for $\gamma = 0.96$; (b) as in (a), but from boxes 3 and 4 (cyan) and C (red) of Fig. 6b for $\gamma = 1.1$. The insets in both panels zoom in on the way that the red dots associated with the chaotic orbits and the cyan dots associated with the nonchaotic orbits are embedded into the global PBA (gray dots).

section 5. Our investigation relies, on the one hand, on the classical FTLEs to measure the rate of divergence of trajectories, but it introduces also a novel metric, namely the time mean σ of the normalized distance δ_n between two initially nearby trajectories. The use of δ_n and σ [cf. Eq. (6)] is required by the extreme complexity of the evolution of the distance between the trajectories: this evolution is far from purely exponential and it involves large variations over different time scales and episodes of synchronization induced by the forcing, as seen in Fig. 8.

In our model, the statistics of an ensemble of trajectories in a chaotic regime does depend on the ensemble of states chosen in the remote past. Figures 6, 7, and 9, in particular, illustrate very well that the model's global PBA—whose existence is rigorously proven in the appendix—contains both chaotic and nonchaotic trajectories.

Both of these types of trajectories have attractor basins that seem to be separated by fractal boundaries: the former fill the global PBA, while the latter form small and smooth subsets of the PBA. This complex, interwoven pattern of rapidly divergent and nondivergent trajectories shows that a time-independent PDF, as often used in predictability studies, is not sufficient to describe the model's long-term behavior or to characterize its predictability.

These intriguing results have been obtained with a highly idealized nonlinear model subject to deterministic aperiodic forcing. As usual in this kind of approach, they raise as many questions as they answer about the broader issues of climate modeling and climate predictability. The two most urgent questions for the climate sciences are these:

- To which extent is this simple model's behavior characteristic of a wide class of nonautonomous dynamical systems, whether deterministic or stochastic?
- How relevant is this class to climate modeling and climate predictability studies?

Again as usual, these questions require one to climb the rungs of a hierarchy of successively more complex and detailed climate models (Ghil 2001; Dijkstra and Ghil 2005; Ghil 2015, and references therein). Naturally, introducing noise in the forcing may substantially modify the system's behavior: a random dynamical system extension of the present study is in progress.

Acknowledgments. SP and MG would like to thank the TEMASAV Project of the Regione Campania of Italy (POR Campania FSE 2007/2013) and the coordinator, Giancarlo Spezie, for having supported exchange visits between the Environmental Research and Teaching Institute (CERES-ERTI) in Paris and the Department of Science and Technology (DiST) of the University of Naples Parthenope, thus promoting this collaboration. The research herein

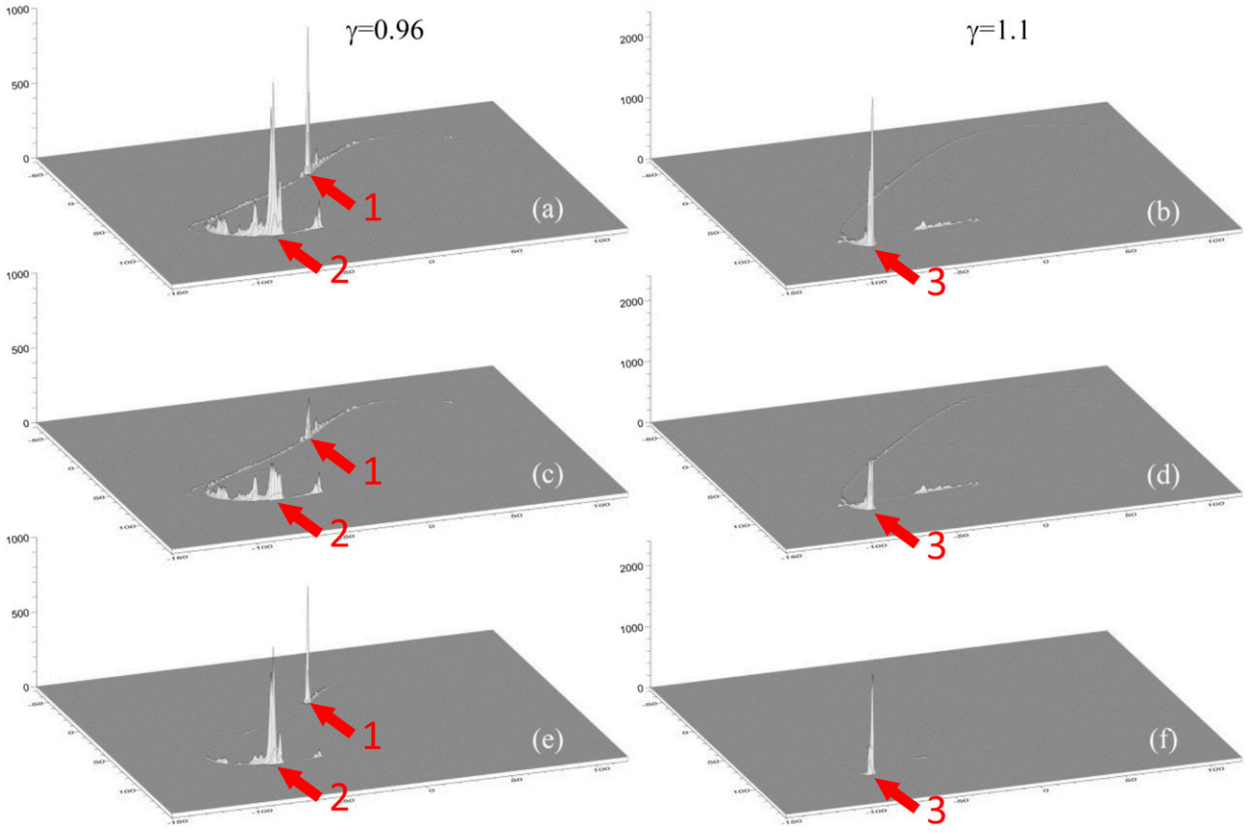

FIG. 10. PDF of localization of the 15 000 trajectories of Figs. 6 and 9 projected onto the (Ψ_1, Ψ_3) plane at $t = 330$ yr, for (a),(c),(e) $\gamma = 0.96$ and (b),(d),(f) $\gamma = 1.1$. The PDF is computed in (a) and (b) from all 15 000 trajectories emanating from Γ; in (c) and (d) only the chaotic trajectories emanating from boxes A and C, respectively, are used; and in (e) and (f) only the nonchaotic trajectories emanating from boxes 1–2 and 3–4, respectively, are used (cf. Fig. 9).

was supported by Grants N00014-12-1-0911 and N00014-16-1-2073 from the Multidisciplinary University Research Initiative (MURI) of the Office of Naval Research and by the U.S. National Science Foundation Grant OCE 1243175 (MDC and MG). The authors wish to thank two anonymous reviewers, whose detailed and constructive comments helped improve the manuscript.

APPENDIX

Existence of a Global Pullback Attractor

We present in this appendix rigorous mathematical results on the existence of pullback attractors (PBAs) in ordinary differential equation (ODE) models—like the one given by Eqs. (1) and (2) here—and, in particular, the conditions on the forcing term $\mathbf{W} = (W_1, \ldots, W_4)$ for such an existence to be guaranteed. General results are known from the specialized literature on the existence of pullback attractors or related invariant manifolds (Kloeden and Rasmussen 2011; Carvalho et al. 2012; Chekroun et al. 2015a,b). For the sake of conciseness and clarity, however, we provide below the main elements of such an existence theory, while emphasizing the energy estimates involved; see also Kondrashov et al. (2015, Theorem 3.1 and Corollary 3.2).

In particular, these existence results are shown to apply to Eqs. (1) and (2) considered in the main text. We mention also that the approach presented below can be adapted to the infinite-dimensional setting and thus to the original two-dimensional quasigeostrophic partial differential equation model, by working in the appropriate function spaces to define the corresponding solutions.

The less mathematically inclined reader can skip appendix section a and proceed directly to section b.

a. Rigorous mathematical background

In what follows X denotes the Euclidean space $\mathbb{R}^d$ ($d \geq 1$), endowed with its natural inner product $\langle \cdot, \cdot \rangle$, and

$\mathscr{B}[0, r(t)]$ denotes the closed ball in X centered at zero, with time-dependent radius $r(t) > 0$.

Theorem 1

Consider the following evolution equation for $\Psi \in X$,

$$\frac{d\Psi}{dt} + L\Psi + B(\Psi, \Psi) = W(t), \tag{A1}$$

for which the initial value problem with $\Psi(0) = \Psi_0$ possesses a unique global solution for any $\Psi_0 \in X$.

Assume that the bilinear term B is energy preserving, that is,

$$\langle B(\Psi, \Psi), \Psi \rangle = 0, \quad \text{for all} \quad \Psi \in X, \tag{A2}$$

and that there exists $\alpha > 0$ such that, for all $\Psi \in X$,

$$\langle L\Psi, \Psi \rangle \geq \alpha \|\Psi\|^2. \tag{A3}$$

Suppose furthermore that $\mathbf{W}$ belongs to $L^2_{\text{loc}}(\mathbb{R}, X)$—the space of X-valued, locally square-integrable functions—and that

$$\int_{-\infty}^{t} e^{\sigma s} \|\mathbf{W}(s)\|^2 \, ds < \infty, \quad \text{for all} \quad t \in \mathbb{R}, \tag{A4}$$

with

$$\sigma = 2(\alpha - \varepsilon), \tag{A5}$$

for some $\varepsilon > 0$ such that $\alpha > \varepsilon$.

Then the propagator U associated with (A1) possesses a unique pullback attractor that pullback attracts any time-dependent set $\mathscr{D}(t)$ such that $\mathscr{D}(t) \subset \mathscr{B}[0, r_\sigma(t)]$, with $r_\sigma(t)$ that satisfies the growth condition

$$\lim_{t \to -\infty} e^{\sigma t} r_\sigma^2(t) = 0. \tag{A6}$$

REMARK 1

Inequality (A3) states that the linear terms in Eq. (1) include dissipative effects.

REMARK 2

(i) We recall that a propagator on X is a two-parameter family of continuous mappings $U(t, \tau): X \to X$, such that $U(\tau, \tau)$ is the identity operator in X, $U(\tau, \tau)x = x$, and that the "multiplication rule"

$$U(t, \tau) = U(t, s)U(s, \tau) \quad \text{for all} \quad \tau \leq s \leq t \tag{A7}$$

applies. It is trivial to show that when a nonautonomous ODE system, such as Eq. (A1), possesses a unique global solution for any $\Psi_0 \in X$, then a propagator U is well defined and is actually given by $U(t, \tau)\Psi_0 := \Psi(t, \tau; \Psi_0)$, where $\Psi(t, \tau; \Psi_0)$ denotes the solution at time t of Eq. (A1) that emanates from Ψ_0 at time $\tau \leq t$.

(ii) A time-dependent set $\mathscr{A}(t)$ is said to pullback attract the time-dependent set $\mathscr{D}(t)$ if

$$\lim_{\tau \to -\infty} \text{dist}_X[U(t, \tau)\mathscr{D}(\tau), \mathscr{A}(t)] = 0, \quad \text{for all} \quad t, \tag{A8}$$

where dist_X denotes the Hausdorff semidistance in X (Carvalho et al. 2012; Chekroun et al. 2011).

Proof

Let us multiply Eq. (A1) by Ψ. Energy conservation by the quadratic term [cf. Eq. (A2)] then yields

$$\frac{1}{2}\frac{d\|\Psi\|^2}{dt} + \langle L\Psi, \Psi \rangle = \langle \mathbf{W}, \Psi \rangle. \tag{A9}$$

By using the dissipativity condition of Eq. (A3) on $\langle L\Psi, \Psi \rangle$ and Young's inequality [Brézis 2010, ch. 2; see Eq. (2) therein and footnote on p. 92] on $\langle \mathbf{W}, \Psi \rangle$, we obtain that, for all $\varepsilon > 0$, there exists a constant $C_\varepsilon > 0$ such that

$$\frac{d\|\Psi\|^2}{dt} + 2(\alpha - \varepsilon)\|\Psi\|^2 \leq C_\varepsilon \|\mathbf{W}\|^2. \tag{A10}$$

Now by choosing ε sufficiently small for $\sigma = 2(\alpha - \varepsilon) > 0$ to hold, we obtain, after integration over $[\tau, t]$,

$$\|\Psi(t)\|^2 \leq e^{-\sigma(t-\tau)}\|\Psi(\tau)\|^2 + C_\varepsilon e^{-\sigma t} \int_\tau^t e^{\sigma s} \|\mathbf{W}(s)\|^2 \, ds. \tag{A11}$$

If $\Psi(\tau) \in \mathscr{D}(\tau) \subset \mathscr{B}[0, r_\sigma(\tau)]$ with r_σ that satisfies the slow-growth condition of Eq. (A6), then the first term on the right-hand side converges to zero as $\tau \to -\infty$, ensuring thus the existence of a dissipation time $\tau_0(t)$ such that, for all $\tau \leq \tau_0(t)$,

$$\|\Psi(t)\|^2 \leq 2C_\varepsilon e^{-\sigma t} \int_{-\infty}^{t} e^{\sigma s} \|\mathbf{W}(s)\|^2 \, ds \equiv R(t). \tag{A12}$$

We have thus proved that $U(t, \tau)\mathscr{D}(\tau) \subset \mathscr{B}[0, R(t)]$ for $\tau \leq \tau_0(t)$, ensuring in turn the desired pullback dissipation. The existence and uniqueness proceed then from this dissipation property and the theory of pullback attractors [e.g., Carvalho et al. (2012)]. ∎

b. Interpretation

We provide here some interpretations of the application of theorem 1 in the context of our idealized

climate model governed by Eqs. (1) and (2). First, the dissipativity parameter α of condition (A3) above is given here by

$$\alpha = \min_{\lambda \in \sigma(L)} [\mathscr{R}e(\lambda)], \tag{A13}$$

where $\sigma(L)$ denotes the spectrum of the linear operator L. For the parameter regime presented in the main text, we find $\alpha = 1.1487 \times 10^{-5}$.

The result of theorem 1 states thus that, for any forcing $\mathbf{W}$ for which σ defined in (A5) is strictly positive, the double-gyre ocean model of Eq. (1) possesses a pullback attractor in the sense of theorem 1. The constant σ in Eq. (A11) is a measure of the rate of pullback dissipation. This constant is very small, on the order of 10^{-5}, which helps explain, as we shall see, the complexity of the model's phase portrait.

The identity (A8) means that $\mathscr{A}(t)$ attracts—with respect to the Hausdorff semidistance and in a pullback sense—any time-dependent set $\mathscr{D}(\tau)$ of initial states at time τ, as they evolve with the action of the propagator $U(t, \tau)$ forward in the time t and as the pullback time τ is sent further and further away into the past.

However, the Hausdorff semidistance is not a distance in the classical sense. For instance, $\mathrm{dist}_X(\mathscr{E}, \mathscr{F}) = 0$ implies that the set $\mathscr{E}$ is included in the set $\mathscr{F}$, but does not guarantee the converse. So if the global attractor $\mathscr{A}(t)$ turns out to be the union of a strange part and of some topologically simpler parts, such as fixed points or periodic orbits, it is definitely possible to have pullback attraction toward the global PBA $\mathscr{A}(t)$, while single trajectories land in different regions of $\mathscr{A}(t)$ that are either chaotic or not. We are then back, in a pullback setting, to the notion of local attractors that compose the global attractor and that can be of topologically very different natures. In the autonomous context, such coexistence of topologically distinct local attractors is well known in the climate sciences (Ghil and Childress 1987; Dijkstra and Ghil 2005; Simonnet et al. 2005, 2009, and references therein), while it is also observed in the numerical results of Figs. 5 and 6 herein for the present ocean model.

As shown in these figures, the boundaries between the corresponding local basins of attractions, as measured with the metrics of section 5, are seemingly intricate and strongly suggest that these objects have fractal features. An attractor basin of chaotic solutions being separated by a fractal boundary from the attractor basin of a fixed point has been documented in a quadratic autonomous model governed by four ODEs that arises in population dynamics; see Fig. 5a in Roques and Chekroun (2011).

In that ecological model, however, no abutting of two different attractor basins of chaotic regions on the global attractor is present. A key difference between the ocean model studied herein and the population dynamics model of Roques and Chekroun (2011) lies in the quadratic terms here being energy preserving [cf. Eq. (A2)], while this is not the case in population dynamics.

There is, therefore, a Hamiltonian skeleton here that may help explain the difference between the two phase portraits: The pullback dissipation being very small argues for the asymptotic trajectories—in spite of the dissipative nature of the dynamics—lying quite close to this skeleton. It is thus not surprising to recover interleaved chaotic islands, as shown in Fig. 6. In the autonomous context, the effects of small dissipation have been studied by Ghil and Wolansky (1992), Feudel and Grebogi (1997), and Seoane et al. (2007), among others.

REFERENCES

Arnold, L., 1998: *Random Dynamical Systems.* Springer, 586 pp.

Bódai, T., and T. Tél, 2012: Annual variability in a conceptual climate model: Snapshot attractors, hysteresis in extreme events, and climate sensitivity. *Chaos*, **22**, 023110, doi:10.1063/1.3697984.

——, G. Károlyi, and T. Tél, 2011: A chaotically driven model climate: Extreme events and snapshot attractors. *Nonlin. Processes Geophys.*, **18**, 573–580, doi:10.5194/npg-18-573-2011.

——, ——, and ——, 2013: Driving a conceptual model climate by different processes: Snapshot attractors and extreme events. *Phys. Rev. E*, **87**, 022822, doi:10.1103/PhysRevE.87.022822.

Brézis, H., 2010: *Functional Analysis, Sobolev Spaces and Partial Differential Equations.* Springer, 600 pp.

Carvalho, A., J. A. Langa, and J. Robinson, 2012: *Attractors for Infinite-Dimensional Non-Autonomous Dynamical Systems.* Springer, 412 pp.

Chang, C. P., M. Ghil, M. Latif, and J. M. Wallace, Eds., 2015: *Climate Change: Multidecadal and Beyond*. World Scientific, 388 pp.

Chao, Y., M. Ghil, and J. C. McWilliams, 2000: Pacific interdecadal variability in this century's sea surface temperatures. *Geophys. Res. Lett.*, **27**, 2261–2264, doi:10.1029/1999GL011324.

Chekroun, M. D., E. Simonnet, and M. Ghil, 2011: Stochastic climate dynamics: Random attractors and time-dependent invariant measures. *Physica D*, **240**, 1685–1700, doi:10.1016/j.physd.2011.06.005.

——, H. Liu, and S. Wang, 2015a: *Approximation of Stochastic Invariant Manifolds: Stochastic Manifolds for Nonlinear SPDEs I.* Springer Briefs in Mathematics, Springer, 127 pp.

——, ——, and ——, 2015b: *Stochastic Parameterizing Manifolds and Non-Markovian Reduced Equations: Stochastic Manifolds for Nonlinear SPDEs II.* Springer Briefs in Mathematics, Springer, 129 pp.

Crucifix, M., 2012: Oscillators and relaxation phenomena in Pleistocene climate theory. *Philos. Trans. Roy. Soc. London*, **370A**, 1140–1165, doi:10.1098/rsta.2011.0315.

De Saedeleer, B., M. Crucifix, and S. Wieczorek, 2013: Is the astronomical forcing a reliable and unique pacemaker for climate? A conceptual model study. *Climate Dyn.*, **40**, 273–294, doi:10.1007/s00382-012-1316-1.

Dijkstra, H. A., and M. Ghil, 2005: Low-frequency variability of the large-scale ocean circulation: A dynamical systems approach. *Rev. Geophys.*, **43**, RG3002, doi:10.1029/2002RG000122.

D'Ovidio, F., J. Iserne-Fontanet, C. Lopez, E. Hernández-García, and E. García-Ladon, 2009: Comparison between Eulerian diagnostics and finite-size Lyapunov exponents computed from altimetry in the Algerian basin. *Deep-Sea Res. I*, **56**, 15–31, doi:10.1016/j.dsr.2008.07.014.

Drótos, G., T. Bódai, and T. Tél, 2015: Probabilistic concepts in a changing climate: A snapshot attractor picture. *J. Climate*, **28**, 3275–3288, doi:10.1175/JCLI-D-14-00459.1.

Eckmann, J.-P., and D. Ruelle, 1985: Ergodic theory of chaos and strange attractors. *Rev. Mod. Phys.*, **57**, 617–656, doi:10.1103/RevModPhys.57.617.

Feudel, U., and C. Grebogi, 1997: Multistability and the control of complexity. *Chaos*, **7**, 597–604, doi:10.1063/1.166259.

Ghil, M., 2001: Hilbert problems for the geosciences in the 21st century. *Nonlinear Processes Geophys.*, **8**, 211–222, doi:10.5194/npg-8-211-2001.

——, 2015: A mathematical theory of climate sensitivity or, how to deal with both anthropogenic forcing and natural variability? *Climate Change: Multidecadal and Beyond*, C. P. Chang et al., Eds., World Scientific, 31–51.

——, 2016: The wind-driven ocean circulation: Applying dynamical systems theory to a climate problem. *Discrete Contin. Dyn. Syst.*, in press.

——, and S. Childress, 1987: *Topics in Geophysical Fluid Dynamics: Atmospheric Dynamics, Dynamo Theory and Climate Dynamics.* Springer-Verlag, 512 pp.

——, and G. Wolansky, 1992: Non-Hamiltonian perturbations of integrable systems and resonance trapping. *SIAM J. Appl. Math.*, **52**, 1148–1171, doi:10.1137/0152068.

——, and A. W. Robertson, 2002: "Waves" vs. "particles" in the atmosphere's phase space: A pathway to long-range forecasting? *Proc. Natl. Acad. Sci. USA*, **99** (Suppl. 1), 2493–2500, doi:10.1073/pnas.012580899.

——, M. D. Chekroun, and E. Simonnet, 2008: Climate dynamics and fluid mechanics: Natural variability and related uncertainties. *Physica D*, **237**, 2111–2126, doi:10.1016/j.physd.2008.03.036.

Haller, G., 2001: Distinguished material surfaces and coherent structures in three-dimensional fluid flows. *Physica D*, **149**, 248–277, doi:10.1016/S0167-2789(00)00199-8.

Jiang, S., F.-F. Jin, and M. Ghil, 1995: Multiple equilibria, periodic, and aperiodic solutions in a wind-driven, double-gyre, shallow-water model. *J. Phys. Oceanogr.*, **25**, 764–786, doi:10.1175/1520-0485(1995)025<0764:MEPAAS>2.0.CO;2.

Kloeden, P. E., and M. Rasmussen, 2011: *Nonautonomous Dynamical Systems*. American Mathematical Society, 264 pp.

Kondrashov, D., M. D. Chekroun, and M. Ghil, 2015: Data-driven non-Markovian closure models. *Physica D*, **297**, 33–55, doi:10.1016/j.physd.2014.12.005.

Legras, B., and M. Ghil, 1985: Persistent anomalies, blocking and variations in atmospheric predictability. *J. Atmos. Sci.*, **42**, 433–471, doi:10.1175/1520-0469(1985)042<0433:PABAVI>2.0.CO;2.

Lenton, T. M., H. Held, E. Kriegler, J. Hall, W. Lucht, S. Rahmstorf, and H. Schellnhuber, 2008: Tipping elements in the earth's climate system. *Proc. Natl. Acad. Sci. USA*, **105**, 1786–1793, doi:10.1073/pnas.0705414105.

Lorenz, E. N., 1963: Deterministic nonperiodic flow. *J. Atmos. Sci.*, **20**, 130–141, doi:10.1175/1520-0469(1963)020<0130:DNF>2.0.CO;2.

——, 1982: Low-order models of atmospheric circulations. *J. Meteor. Soc. Japan*, **60**, 255–267.

——, 1984: Irregularity: A fundamental property of the atmosphere. *Tellus*, **36A**, 98–110, doi:10.1111/j.1600-0870.1984.tb00230.x.

Mann, M. E., R. S. Bradley, and M. K. Hughes, 1998: Global-scale temperature patterns and climate forcing over the past six centuries. *Nature*, **392**, 779–787, doi:10.1038/33859.

Martinson, D. G., K. Bryan, M. Ghil, M. Hall, T. R. Karl, E. S. Sarachik, S. Sorooshian, and L. D. Talley, Eds., 1995: *Natural Climate Variability on Decade-to-Century Time Scales*. National Academies Press, 644 pp.

Nese, J., 1989: Quantifying local predictability in phase space. *Physica D*, **35**, 237–250, doi:10.1016/0167-2789(89)90105-X.

Olbers, D., 2001: A gallery of simple models from climate physics. *Stochastic Climate Models*, Vol. 49, *Progress in Probability*, P. Imkeller and J. von Storch, Eds., Springer, 3–63.

Ott, E., 2002: *Chaos in Dynamical Systems.* Cambridge University Press, 478 pp.

Pierini, S., 2006: A Kuroshio Extension system model study: Decadal chaotic self-sustained oscillations. *J. Phys. Oceanogr.*, **36**, 1605–1625, doi:10.1175/JPO2931.1.

——, 2010: Coherence resonance in a double-gyre model of the Kuroshio Extension. *J. Phys. Oceanogr.*, **40**, 238–248, doi:10.1175/2009JPO4229.1.

——, 2011: Low-frequency variability, coherence resonance, and phase selection in a low-order model of the wind-driven ocean circulation. *J. Phys. Oceanogr.*, **41**, 1585–1604, doi:10.1175/JPO-D-10-05018.1.

——, 2012: Stochastic tipping points in climate dynamics. *Phys. Rev. E*, **85**, 027101, doi:10.1103/PhysRevE.85.027101.

——, 2014a: Ensemble simulations and pullback attractors of a periodically forced double-gyre system. *J. Phys. Oceanogr.*, **44**, 3245–3254, doi:10.1175/JPO-D-14-0117.1.

——, 2014b: Kuroshio Extension bimodality and the North Pacific Oscillation: A case of intrinsic variability paced by external forcing. *J. Climate*, **27**, 448–454, doi:10.1175/JCLI-D-13-00306.1.

——, H. A. Dijkstra, and A. Riccio, 2009: A nonlinear theory of the Kuroshio Extension bimodality. *J. Phys. Oceanogr.*, **39**, 2212–2229, doi:10.1175/2009JPO4181.1.

Pikovsky, A., and J. Kurths, 1997: Coherence resonance in a noise-driven excitable system. *Phys. Rev. Lett.*, **78**, 775–778, doi:10.1103/PhysRevLett.78.775.

Platzman, G., 1960: The spectral form of the vorticity equation. *J. Meteor.*, **17**, 635–644, doi:10.1175/1520-0469(1960)017<0635:TSFOTV>2.0.CO;2.

Rasmussen, M., 2007: *Attractivity and Bifurcation for Nonautonomous Dynamical Systems.* Springer, 217 pp.

Romeiras, F. J., C. Grebogi, and E. Ott, 1990: Multifractal properties of snapshot attractors of random maps. *Phys. Rev. A*, **41**, 784–799, doi:10.1103/PhysRevA.41.784.

Roques, L., and M. D. Chekroun, 2011: Probing chaos and biodiversity in a simple competition model. *Ecol. Complex.*, **8**, 98–104, doi:10.1016/j.ecocom.2010.08.004.

Saltzman, B., 1962: Finite amplitude free convection as an initial value problem. *J. Atmos. Sci.*, **19**, 329–341, doi:10.1175/1520-0469(1962)019<0329:FAFCAA>2.0.CO;2.

Seoane, J. M., M. A. Sanjuán, and Y.-C. Lai, 2007: Fractal dimension in dissipative chaotic scattering. *Phys. Rev. E*, **76**, 016208, doi:10.1103/PhysRevE.76.016208.

Simonnet, E., M. Ghil, and H. Dijkstra, 2005: Homoclinic bifurcations in the quasi-geostrophic double-gyre circulation. *J. Mar. Res.*, **63**, 931–956, doi:10.1357/002224005774464210.

——, H. A. Dijkstra, and M. Ghil, 2009: Bifurcation analysis of ocean, atmosphere and climate models. *Computational Methods for the Ocean and the Atmosphere*, R. Temam and J. J. Tribbia, Eds., North-Holland, 187–229.

Tél, T., and M. Gruiz, 2006: *Chaotic Dynamics: An Introduction Based on Classical Mechanics.* Cambridge University Press, 393 pp.

Vannitsem, S., 2014a: Dynamics and predictability of a low-order wind-driven ocean–atmosphere coupled model. *Climate Dyn.*, **42**, 1981–1998, doi:10.1007/s00382-013-1815-8.

——, 2014b: Stochastic modelling and predictability: Analysis of a low-order coupled ocean–atmosphere model. *Philos. Trans. Roy. Soc.*, **372A**, 20130282, doi:10.1098/rsta.2013.0282.

——, and L. De Cruz, 2014: A 24-variable low-order coupled ocean–atmosphere model: OA-QG-WS v2. *Geosci. Model Dev.*, **7**, 649–662, doi:10.5194/gmd-7-649-2014.